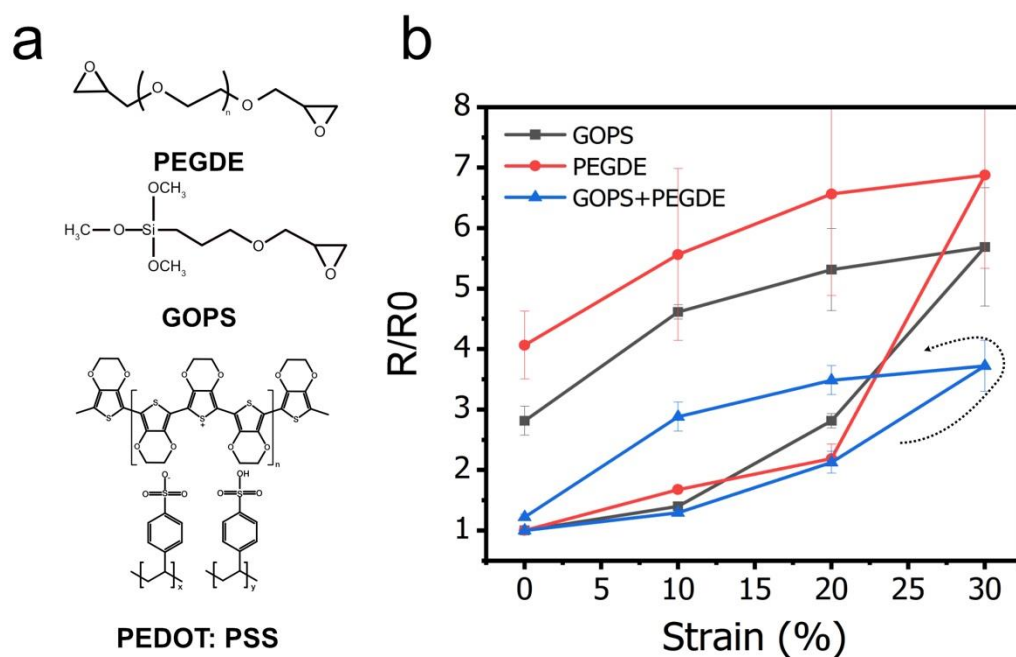# A wearable in-sensor computing platform based on stretchable organic electrochemical transistors

In the format provided by the authors and unedited

Supplementary figure 1. The effect of different crosslinkers on the stretchability of PEDOT: PSS thin films. (a) Chemical structures of PEDOT:PSS and crosslinkers: (3-glycidyloxypropyl) trimethoxysilane (GOPS) and polyethylene glycol diglycidyl ether (PEGDE, Mn ~ 2000). **(b)** Resistance changes of PEDOT: PSS thin films on SEBS substrates under one cycle strain between 0% to 30%. The black line refers to PEDOT:PSS crosslinked with 1 v/v.% GOPS; the red line refers to PEDOT: PSS crosslinked with 1 v/v.% PEGDE; the blue line refers to PEDOT:PSS crosslinked with 0.2 v/v.% GOPS and 0.8 v/v.% PEGDE. Data are presented as mean values with +/- SEM (Standard error of mean); n=7 independent tests.

a

b

c
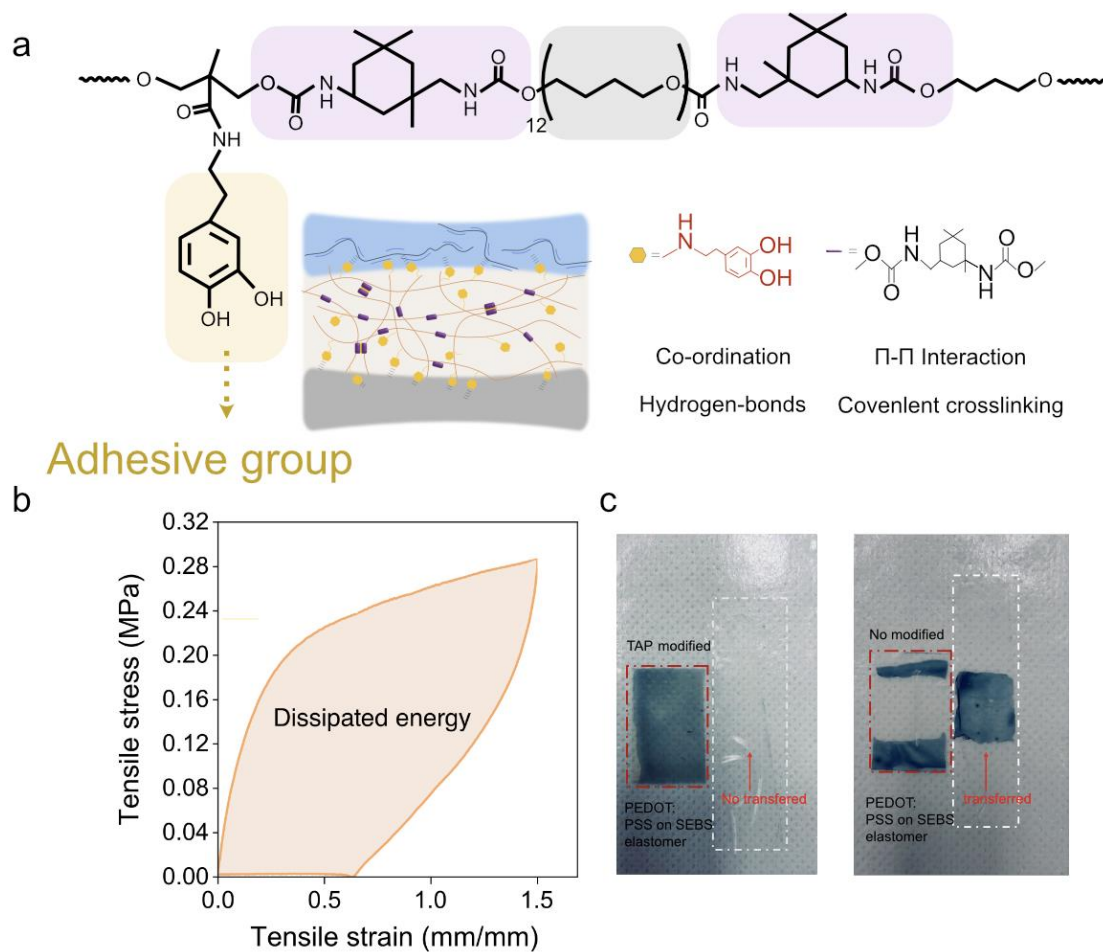
Supplementary figure 2. The design strategy of the tough adhesive polymer (TAP). (a) Molecular structure of TAP. **(b)** The stress-strain curve of TAP shows a large hysteresis loop, indicating efficient energy dissipation through dynamic hydrogen bonding. **(c)** Tape-scratching experiments. Left: PEDOT: PSS coated on TAP-modified SEBS. Right: PEDOT: PSS on SEBS. The results demonstrate TAP improved adhesion between PEDOT: PSS and SEBS.
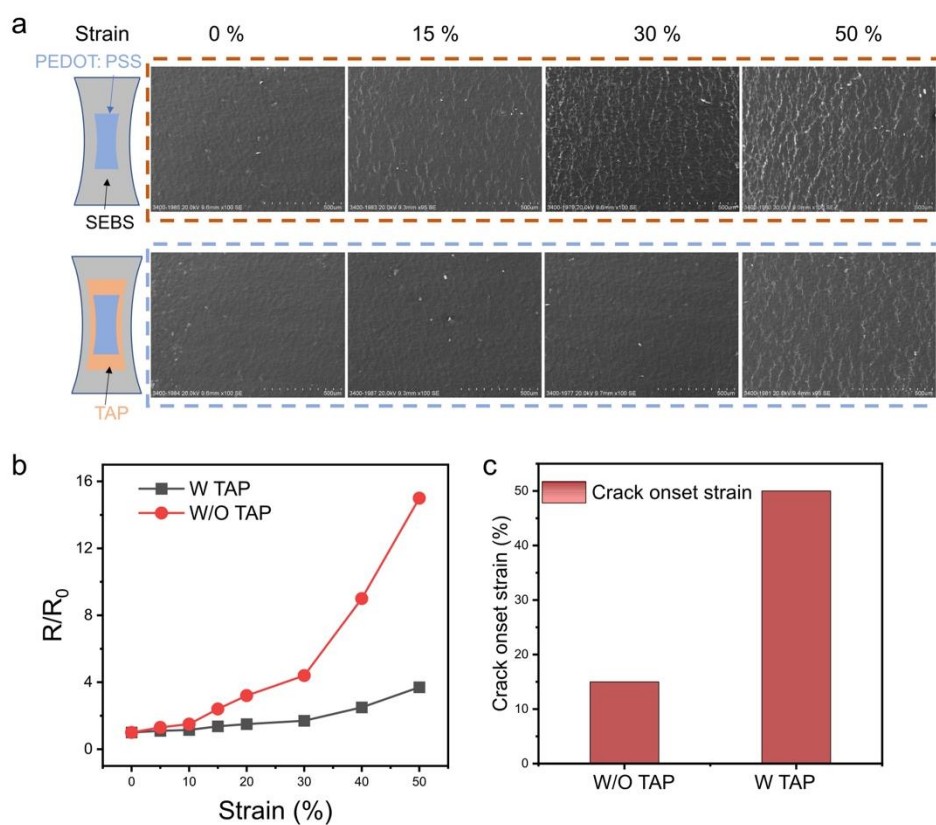
Supplementary figure S3. Effect of TAP adhesive layer on the stretchability of PEDOT:PSS thin film. (a) Scanning electron microscope images of PEDOT:PSS thin films on SEBS and TAP-modified SEBS substrates. **(b)** Resistance changes of PEDOT:PSS thin films under strain (0%-50%). **(c)** Comparison of crack onset strain of PEDOT:PSS thin films with and without TAP modification.
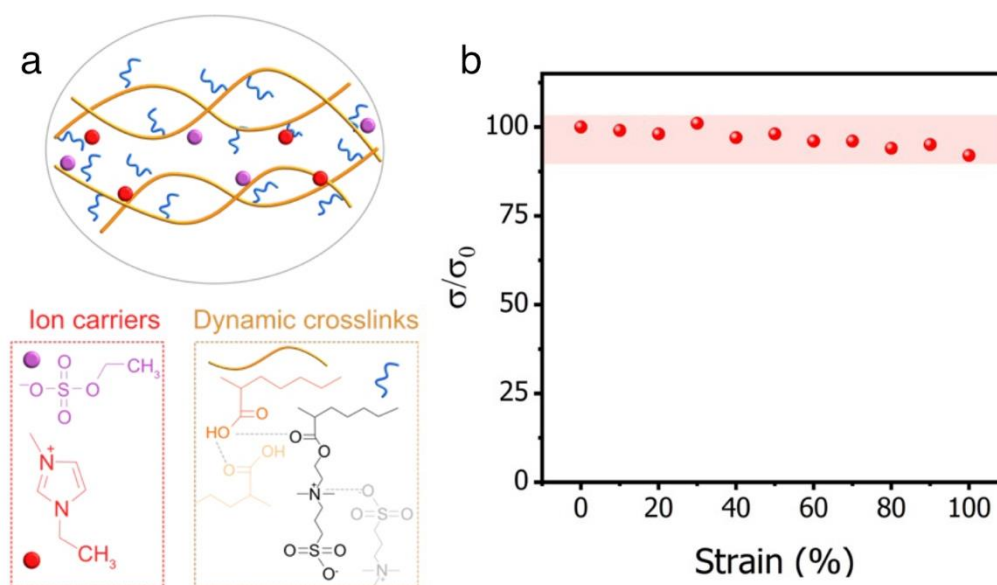
Supplementary figure 4. Design of stretchable iongel electrolytes. (a) Chemical structure of the iongel, featuring a polyzwitterionic network with 3-dimethyl (methacryloyloxyethyl) ammonium propane sulfonate (PDMAPS), a polyanionic network with polyacrylic acid (PAA), and an ionic liquid as the ion carrier. **(b)** Stability of ionic conductivity under different strain values.
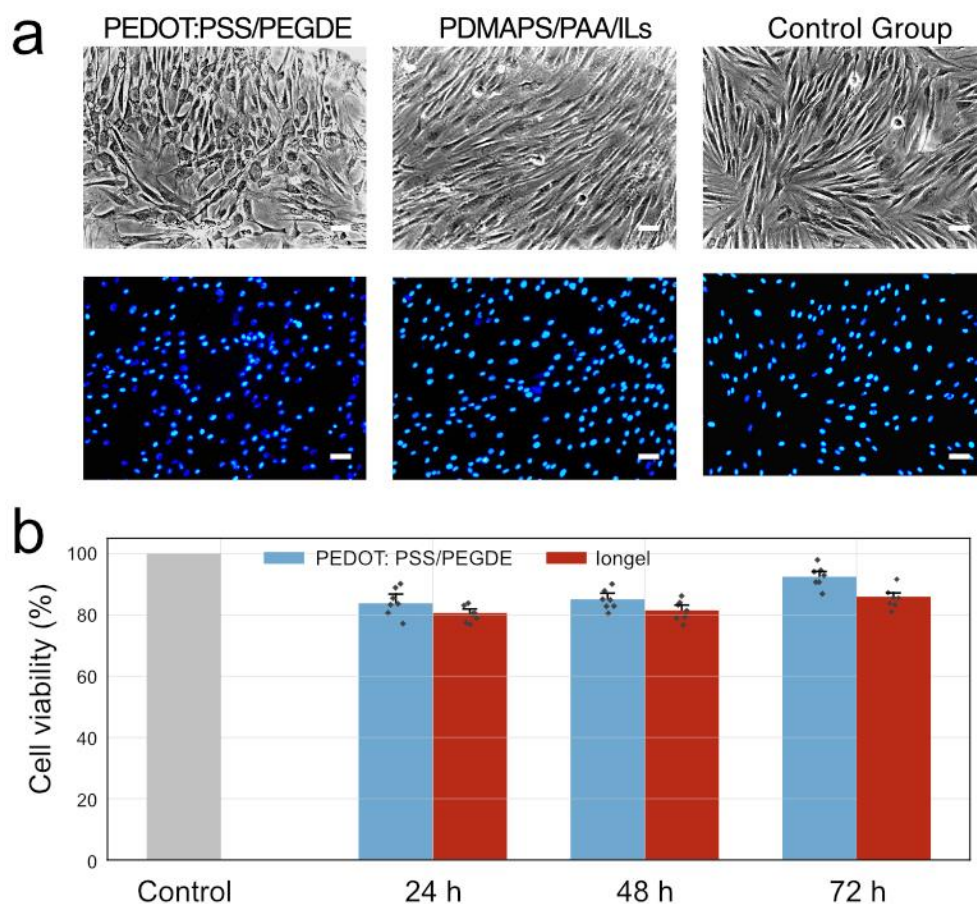
Supplementary figure 5. Biocompatibility tests of the formulated PEDOT:PSS films and the iongel. (a) Optical images (top) and fluorescence microscope images (bottom) of human skin fibroblasts (HSF) on PEDOT:PSS thin film, iongel, and a control group (glass) after 3 days of incubation. Scale bar: 100 μm. **(b)** HSF cell viability after 24, 48, and 72 hours. Data are presented as mean values with +/- SEM; n=7 independent tests.

The biocompatibility of PEDOT: PSS and ion gel was evaluated using HSF. The fibroblasts were cultured in T-25 flasks with a complete culture medium consisting of 89% Dulbecco's Modified Eagle Medium (DMEM), 10% fetal bovine serum (FBS), and 1% penicillin-streptomycin, under a 5% CO_2 atmosphere at 37°C. Upon reaching a confluency of approximately 90%, cells were passaged and subsequently seeded onto 96-well and 12-well plates, which had been previously lined with PEDOT: PSS thin film and ion gel films.

The experiment was designed with three groups: Group A with cells cultured on PEDOT: PSS thin film, Group B on iongel film, and a control group on standard tissue culture plates. Cellular viability was assessed at 24, 48, and 72 hours using the Cell Counting Kit-8 (CCK8) assay, which involved measuring the absorbance at 450 nm with a microplate reader (Multiskan Mk3, Thermo Fisher Scientific). For morphological assessment, cells were fixed with 4% paraformaldehyde after 72 hours of culture and stained with Hoechst 33342. Photomicrographs were taken under both bright field and fluorescent conditions at 100x magnification to evaluate the nuclear integrity and

morphology. All the procedures involving the on-skin attachment of ISOECT array on the human skin followed ethical guidelines, which were approved by The University of Hong Kong (EA230538).
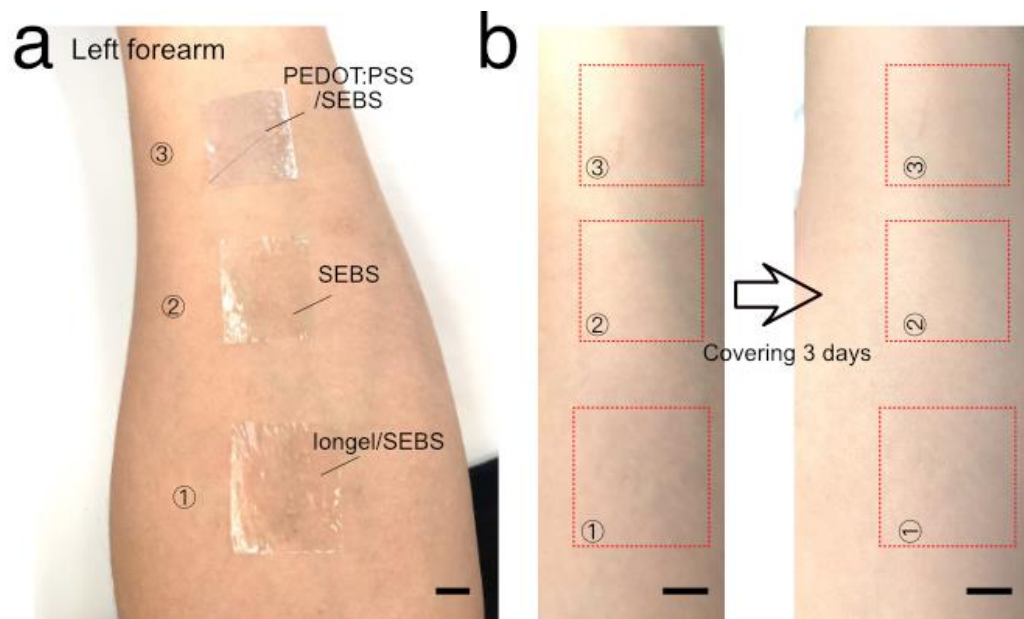
Supplementary figure 6. Skin irritation test. (a) Experimental setup: tested materials (PEDOT: PSS/SEBS, iongel/SEBS) and a control group (SEBS) were attached to the left forearm and secured with medical tape. **(b)** Comparison of skin condition before and after 3 days of contact with the tested materials. Scale bars: 1 cm.
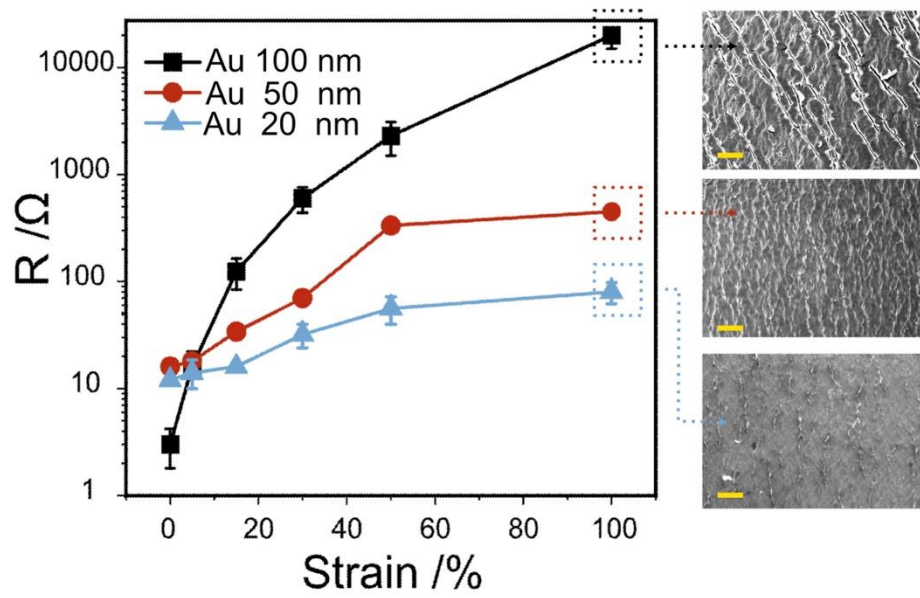
Supplementary figure 7. Stretchability of nano Au on TAP-modified elastomer. (a) Resistance changes of Au thin films (thickness of 100 nm, 50 nm, and 20 nm) under different strain values (n=7). Data are presented as mean values with +/- SEM; n=7 independent test. **(b)** Scanning electron microscopic images of the Au thin film under 100% strain. Scale bar: 100 μm.
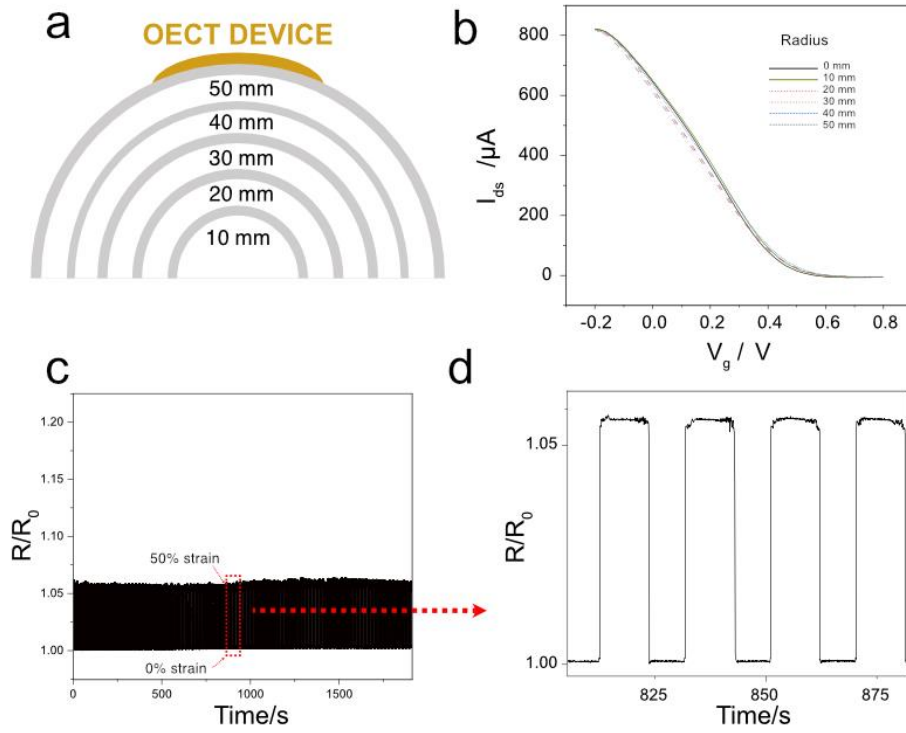
Supplementary figure 8. The electromechanical test of ISOECT. (a) Illustration of experimental setup for the bending test. The device was bent and fixed on a 3D-printed arch-shaped mold with different radii ranging from 10 mm to 50 mm. **(b)** Transfer curves of ISOECTs at different bending states. **(c)** Stability of I_{ds} of ISOECTs within 100 cycles' strain test from 0 % to 50 %, and **(d)** a zoom-in view.
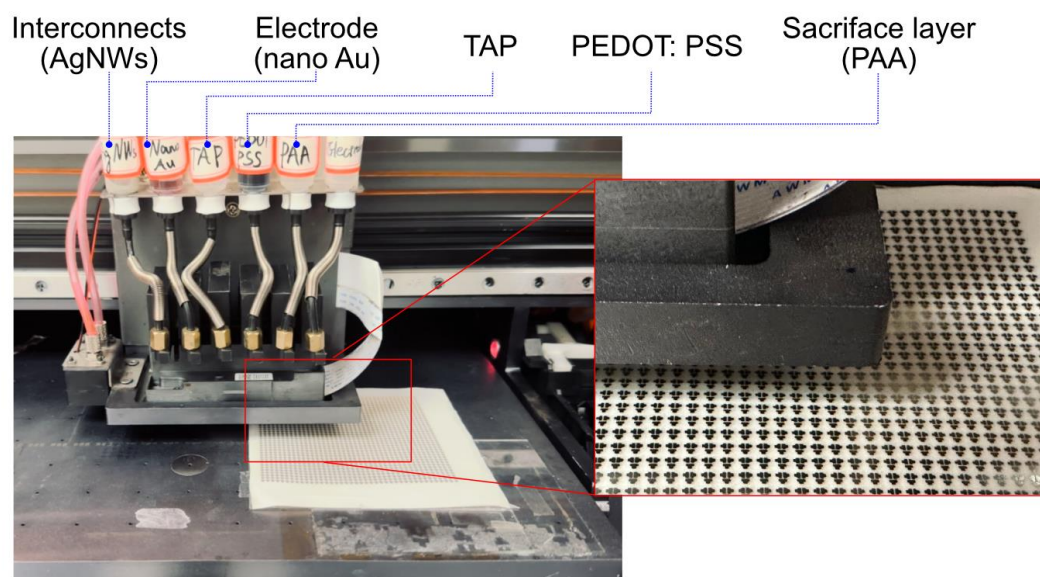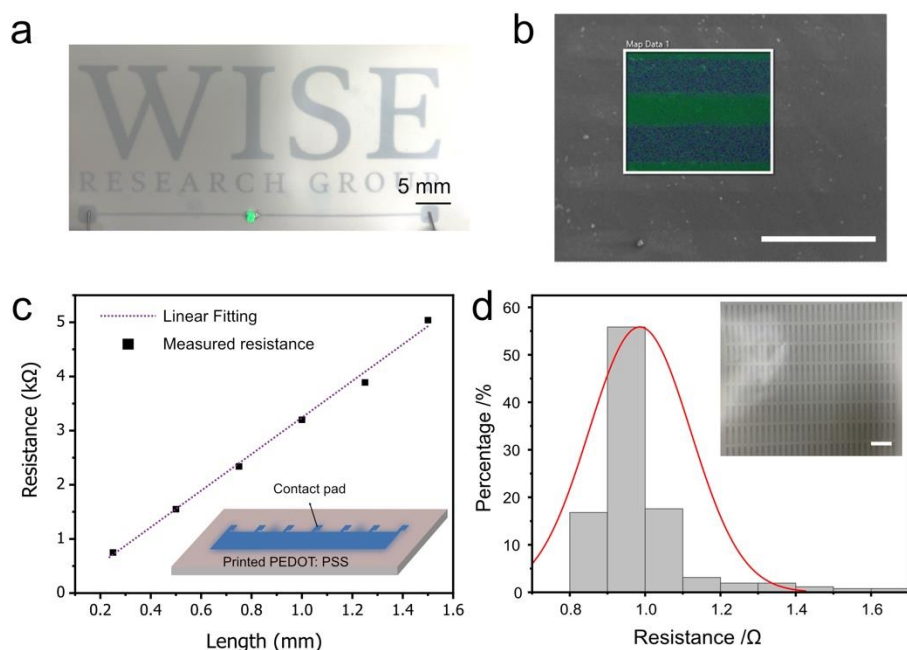
Supplementary figure 9. Optical image of the customized multichannel inkjet printing system for ISOECT fabrication.
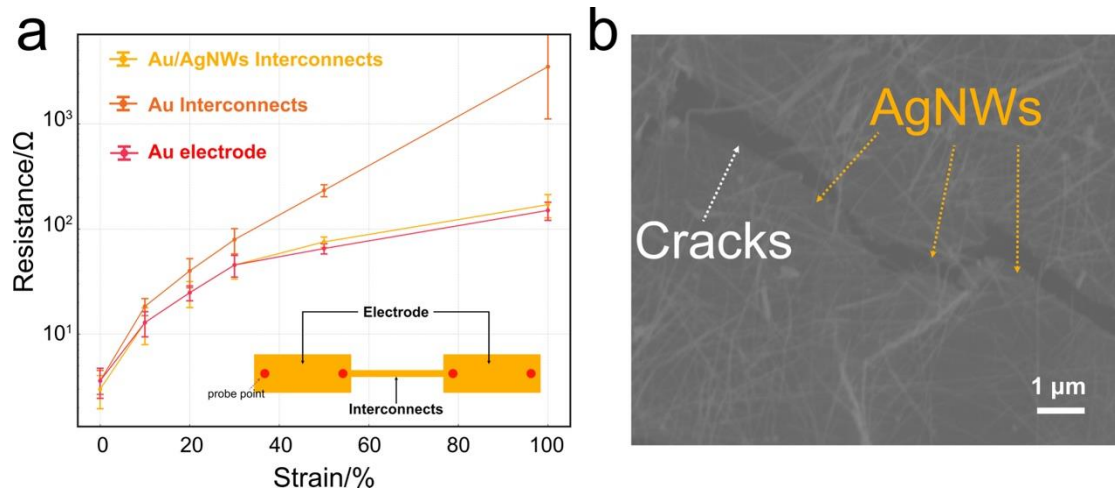
Supplementary figure 10. Interconnects' conductivity under strain. (a) Changes in conductivity of electrodes and interconnects under strain ranging from 0 % to 100%. Data are presented as mean values with +/- SEM; n=7 independent test. **(b)** Scanning electron microscope images of Au/Silver nanowires (AgNWs) interconnect under strain of 100%. The AgNWs can bridge cracked Au (cracking onset strain of 50%), therefore maintaining a high conductivity under strain.
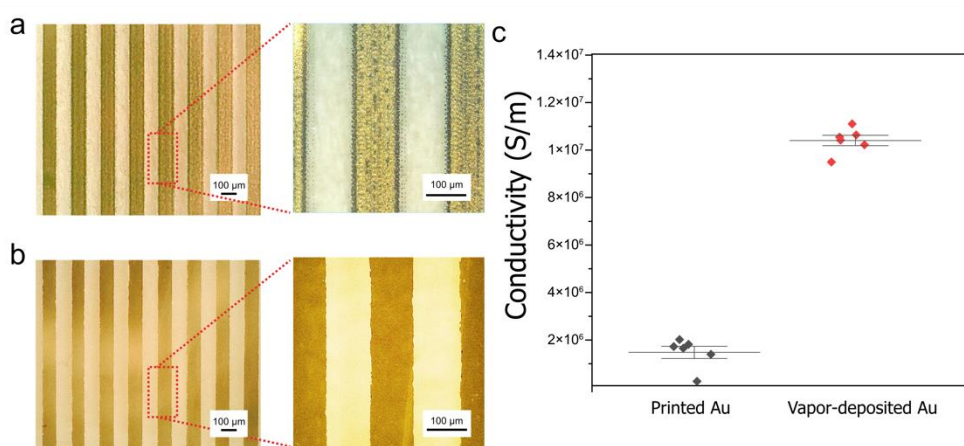
Supplementary figure 11. Comparison of vapor-deposited Au and printed Au electrodes. (a-b) Optical images of printed Au (a) and vapor-deposited Au (b) traces. Scale bar: 100 μm. **(c)** The comparison of conductivity between printed Au, and vapor-deposited Au. Data are presented as mean values with +/- SEM; n=6 independent tests.

Supplementary figure 12. Characterization of inkjet-printed of PEDOT: PSS films. (a) Optical image of inkjet-printed PEDOT: PSS patterns. Scale bar: 5 mm. **(b)** Morphology of the printed PEDOT: PSS test lines. Scale bar: 500 μm. In the energy dispersive spectroscopy (EDS) mapping image, green pixels represent carbon (C), and blue pixels represent sulfur (S), indicating the existence of PEDOT: PSS. **(c)** Correlation between resistance and length of PEDOT: PSS lines. The good linearity indicates a uniform patterning. **(d)** Resistance distribution of printed PEDOT: PSS patterns. Scale bar: 1cm.
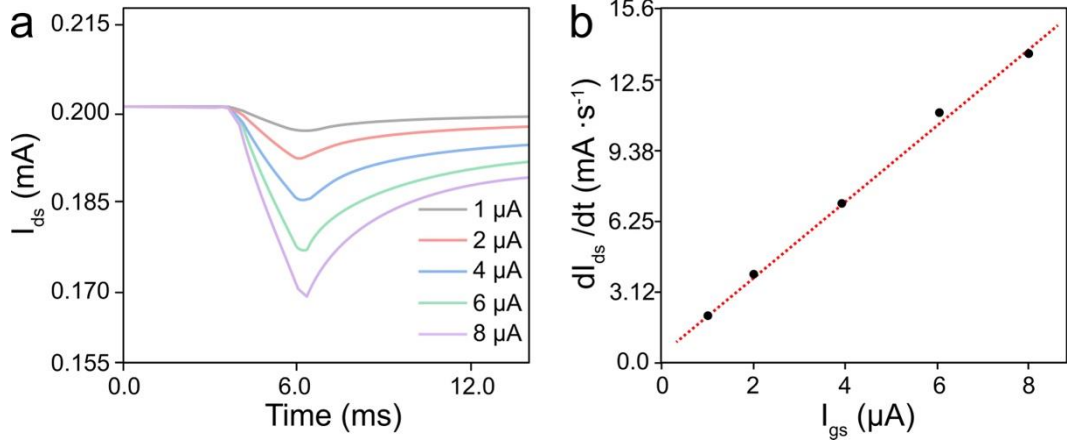
Supplementary figure 13. Mobility test of the ISOECT device. (a) Transient response of ISOECT (W=500 μm, L=100 μm) upon gate current input (I_{gs}, from 1 μA to 8 μA). **(b)** Correlation of current change rate (dI_{ds}/dt) and I_{gs}.

According to the Malliaras-Bernards model,[1] the response of OECT can be understood by considering the OECT consisting of two circuits: the ionic one, where ions are transported between the electrolyte and the channel, and the electronic one where holes are transported in the PEDOT: PSS channel between the source and drain. The ionic circuit is governed by the species of ions and the interface between the electrolyte and channel. The latter can be estimated by driving the OECT with constant gate current and simultaneously measuring the change of source-drain current regarding response time, and the mobility of PEDOT: PSS on both soft and rigid substrate can be calculated via Eq. (1) to Eq. (3):

$$I_{ds}(t, I_{gs}) = I_{ds0} - I_{gs}(f + \frac{t}{\tau_e}) \tag{1}$$

$$\frac{dI_{ds}}{dI_t} = -\frac{I_{gs}}{\tau_e} \tag{2}$$

$$\tau_e = -L^2/uV_{ds} \tag{3}$$

where t is the time, I_{ds} is the source-drain current before application of I_{gs}, f is a proportionality constant to account for the spatial non-uniformity of the de-doping process, τ_e is the electronic transit time, L is the channel length of OECT (100 μm) and V_{ds} is the source-drain voltage (-0.2 V). u denotes the hole mobility of the PEDOT: PSS channel. According to Eq. (1) and (2), we could calculate the electronic transit time from the linear transient response range of I_{ds} in

Supplementary figure 13a. Subsequently, we could extract the mobility ($u \approx 0.8$ cm$^2 \cdot$V$\cdot$s^{-1}) according to Eq. (3).
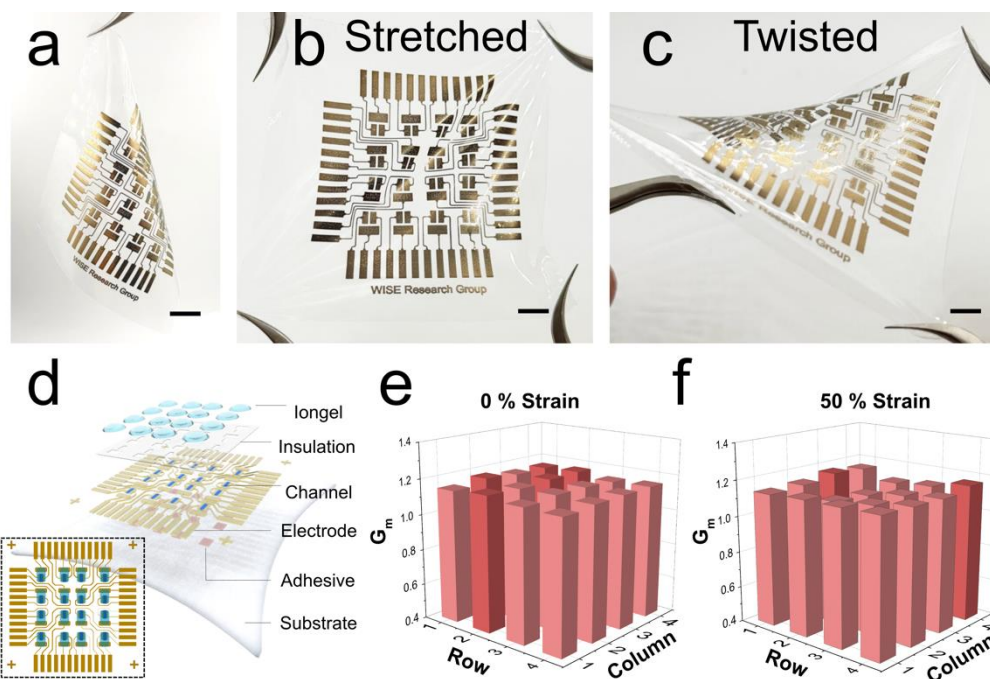
Supplementary figure 14. Stretchability of the ISOECT array (with interconnects). (a-c) Optical images of the 4×4 ISOECT array under different stretching conditions. Scale bar: 5 mm. **(d)** Illustration of the structure of ISOECT array. **(e-f)** Distribution of maximized g_m values of ISOECTs in the array at 0% strain (e) and 50% strain (f).
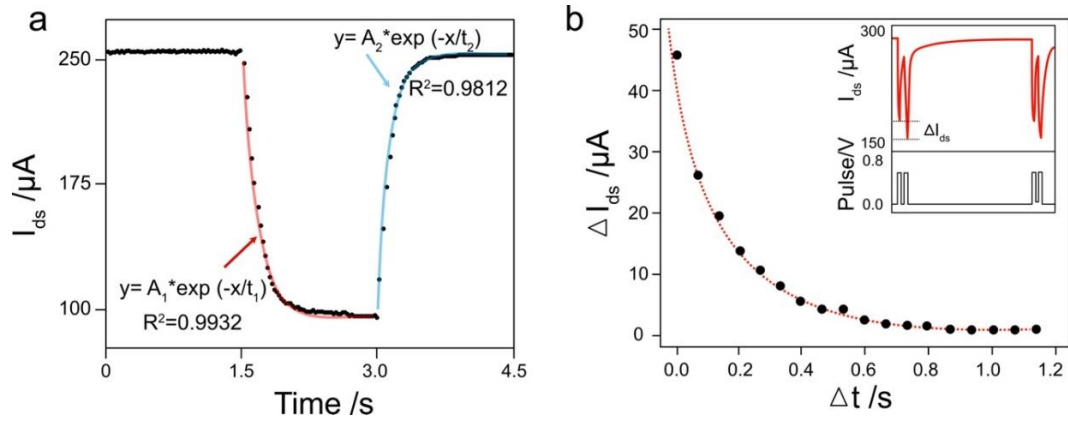
Supplementary figure 15. Nonlinear behavior test of ISOECT. (a) Transient response of the ISOECT, showing typical nonlinear response. **(b)** Short-term depression and paired-pulse facilitation result of the ISOECT.
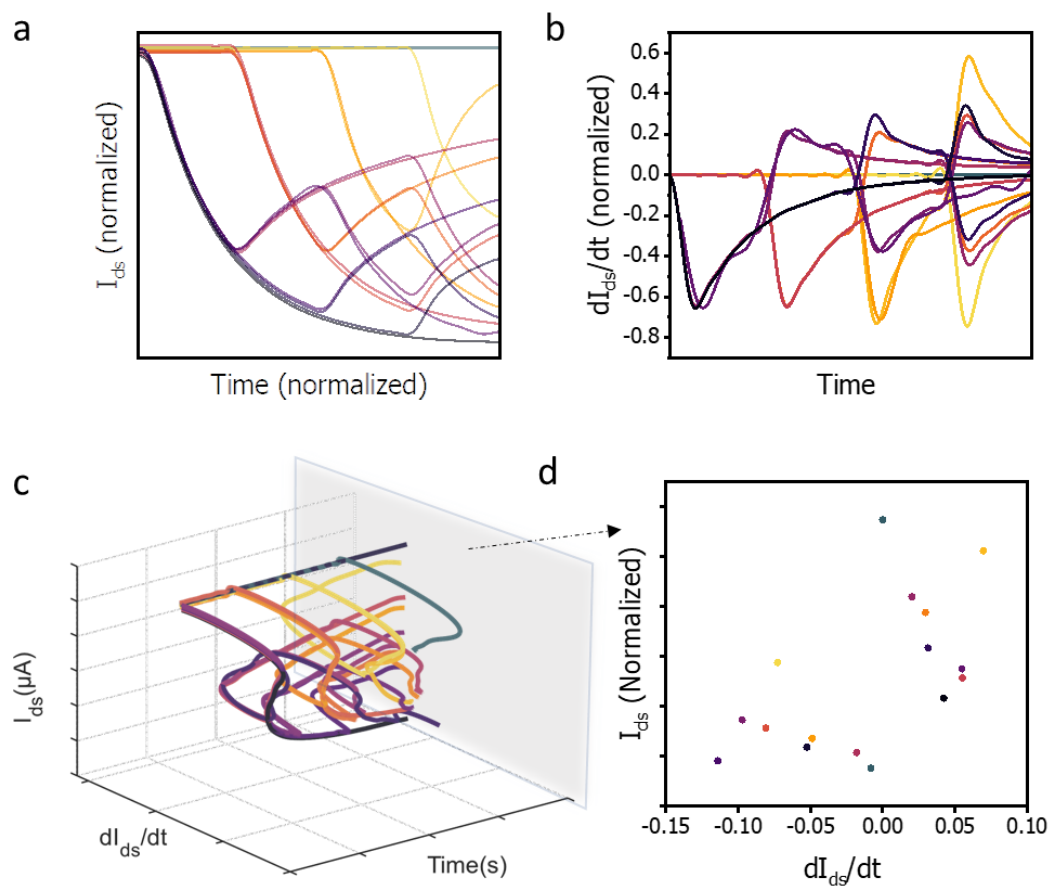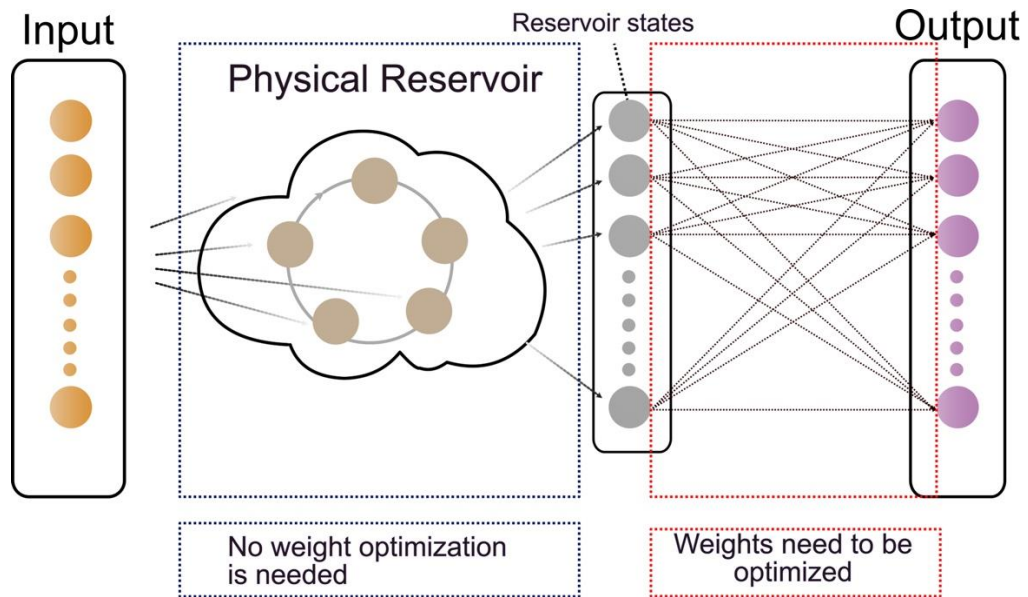
Supplementary figure 16. Reservoir behavior of the ISOECT. (a) Changes in I_{ds} responding to 16 types of inputs, ranging from 0000 to 1111. **(b)** Current change rates over time (dI_{ds}/dt) corresponding to the 16 inputs. **(c)** Evolution of I_{ds} and dI_{ds}/dt over time. **(d)** Cross-sectional plot of (c) at the readout timepoint.
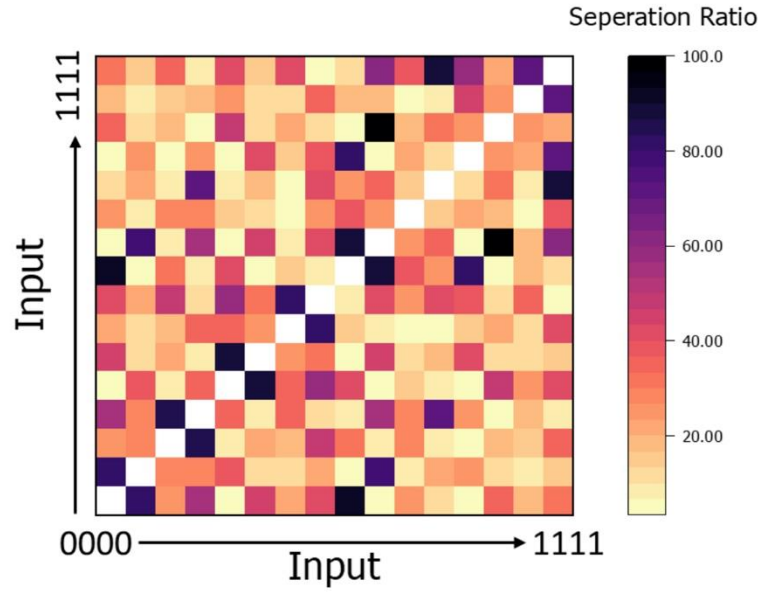
Supplementary figure 17. Separation ratios between inputs and outputs. We use the Manhattan distance metric to assess separation ratios in a 4-bit pulse series with 16 inputs (0000 to 1111), where '0' represents low level and '1' represents high level. The Manhattan distance sums the absolute differences between corresponding bits of input-output pairs. For example, for input 0101 and output 1001, the calculation is |0-1| + |1-0| + |0-0| + |1-1| = 2. Dividing this by the total number of bits (4), the separation ratio is 0.5. Smaller ratios indicate higher similarity, while larger ratios suggest greater dissimilarity.
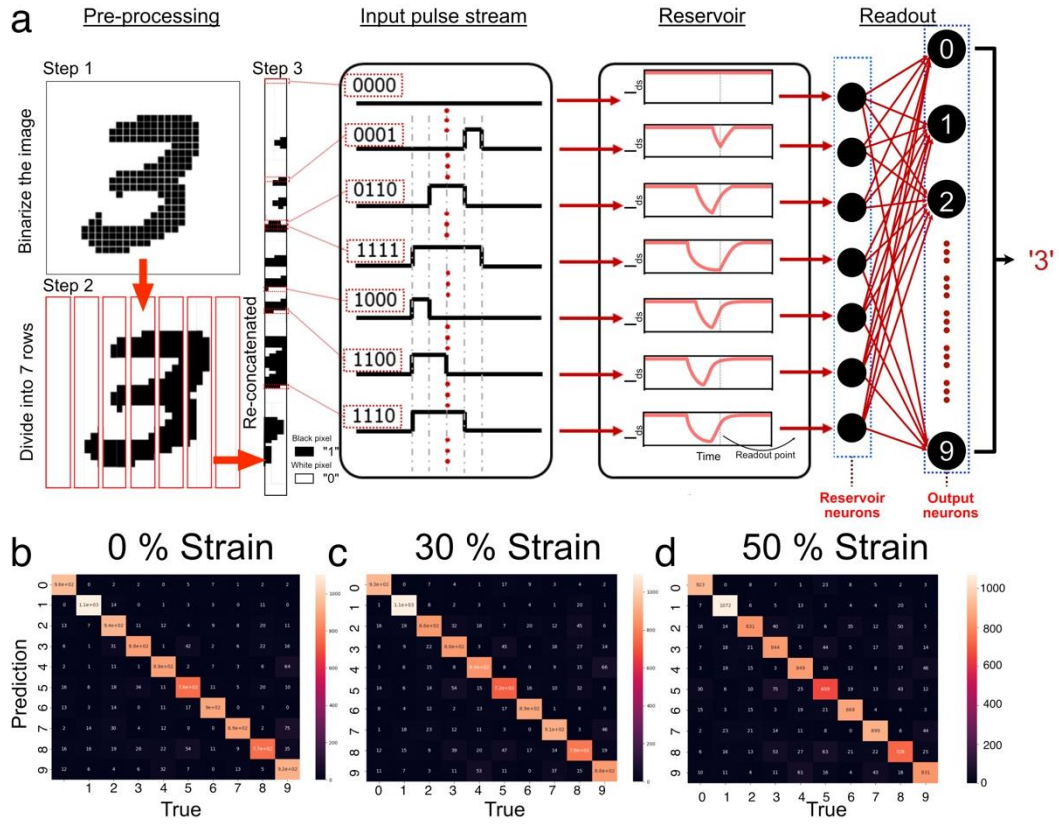
Supplementary figure 18. Handwritten digit recognition using ISOECT-based RC network.
(a) Processing flows. **(b-d)** Simulated prediction results under strain of 0% (b), 30% (c), and 50% (d).

Supplementary figure 19. Schematic of the RC. The RC framework consists of a reservoir layer and an output layer, where only the weights in the output layer need to be trained and optimized.

Table 1. Comparison of RC hardware reported in literatures.

| Device	Write-in mode	Readout voltage (V)	Write-in voltage (V)	Write-in power (nW)	Readout power (nW)	Power consumption (nW)	Stretchable (Y/N)	Stable operation in water (Y/N)	Ref.
ISOECT	Voltage	0.004	0.01	16	20	36	Y	Y	This work
WO*x* memristor	Voltage	0.6	1.4	/	1000	150-1000	N	N	1
SnS memristor	Light	0.5	/	43000	/	~43000	N	N	2
AgNWs network	Voltage	0.1	2	/	/	75000	N	N	3
Ti/TiO*x*/TaO*y*/Pt memrisistor	Voltage	2	2	100	/	50000	N	N	4
WOx-based memristor	Voltage	0.6	3	/	/	300000	N	N	5
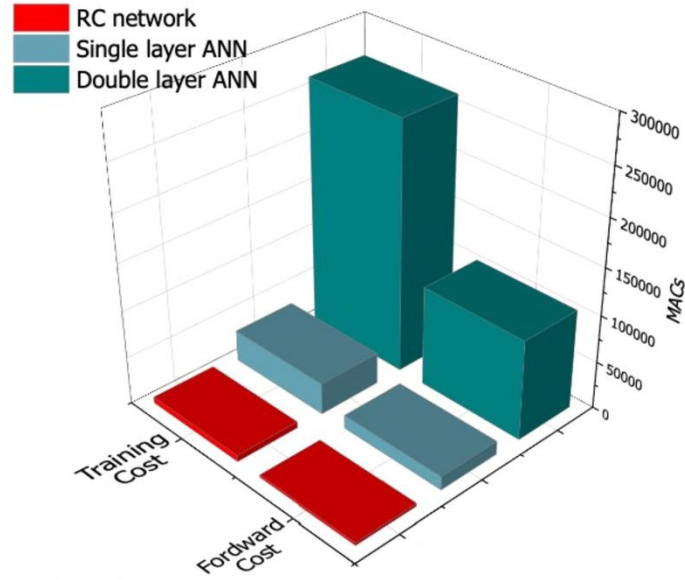
Supplementary figure 20. The comparison of computing cost between our ISOECT RC network and conventional single- and double-layer artificial neuron networks (ANNs).

Supplementary figure 20 compares the number of multiply and accumulate (MAC) operations during training and inference for our ISOECT RC system, a single-layer ANN, and a two-layer ANN. During inference, the number of MAC operations for a single image of a hand-written digit is about 2.9k, significantly less than single-layer ANN (~14.4k) and double-layer ANN (~105.9k). Also, during training, the number of MAC operations of our system is about 6.7k, while that of a single-layer ANN is about 33.3k, and that of a two-layer ANN is about 265.2k.
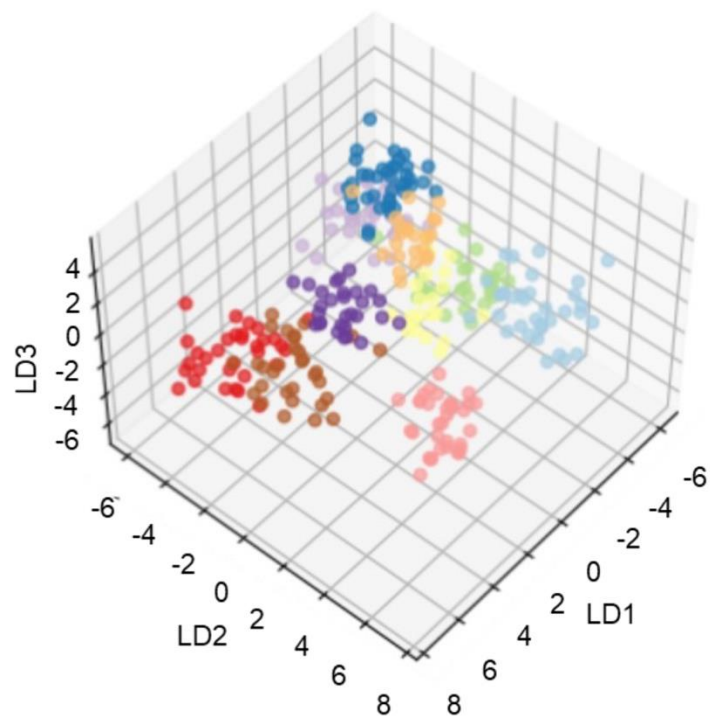
Supplementary figure 21. The 3D visualization of the feature vector distribution via prominent component analysis (PCA). LD: latent dimensions.
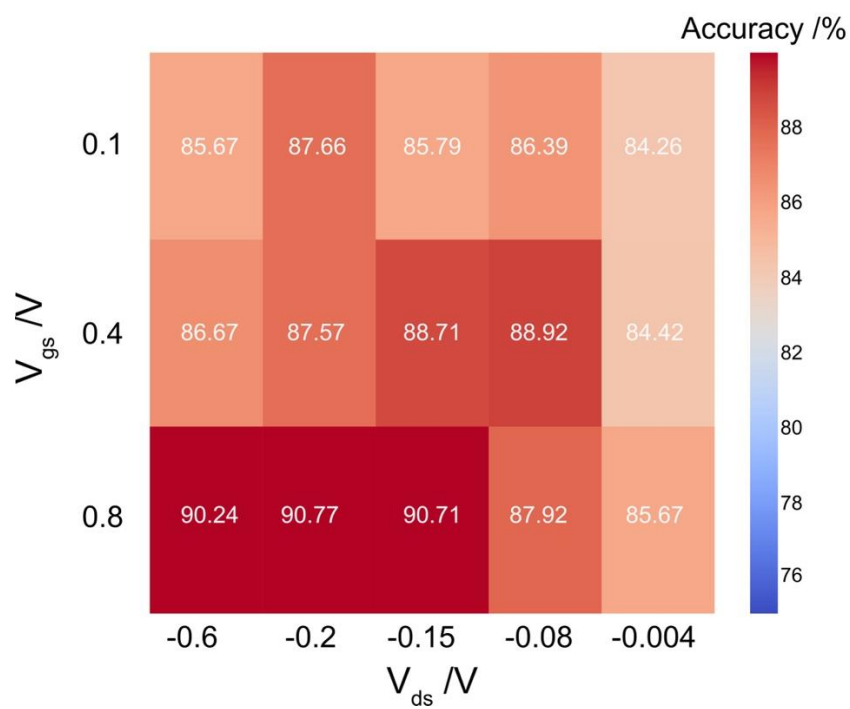
Supplementary figure 22. Heatmap of the prediction accuracy (handing-written digits recognition) for ISOECT RC under different operation voltages.
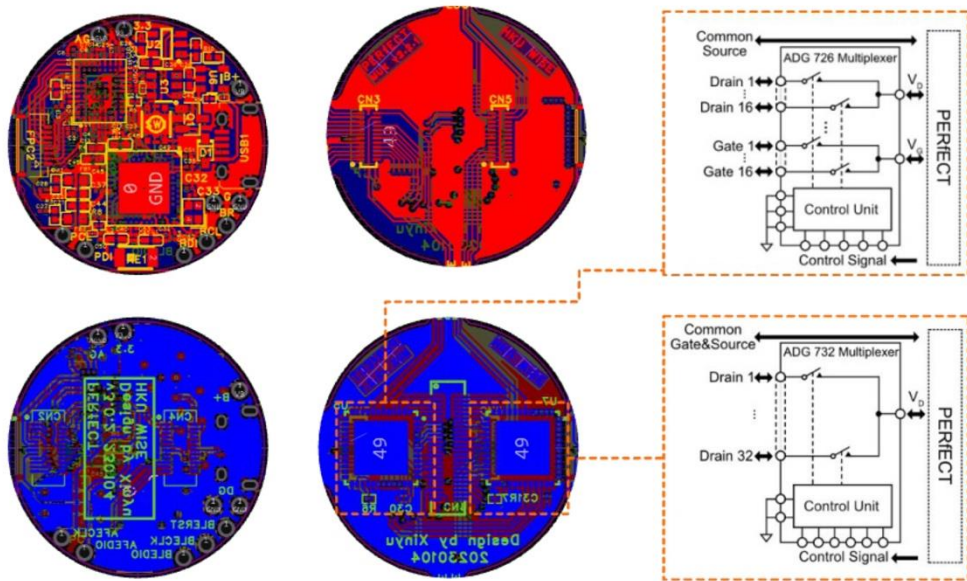
Supplementary figure 23. The extended board for multiplexed OECT characterizations based on the PERfECT readout system. The Multiplexer was customized for PERfECT to control and readout the ISOECT array for sensing and computing. We developed extended circuit boards with CMOS-based 32-channel/16-channel high-speed multiplexers (ADG732 and ADG726) to upgrade "PERfECT" to "PERfECTs". These multiplexers allow the system to record multiple channels within a time window of 100 ns and control the channel-to-channel crosstalk around -72 dB.
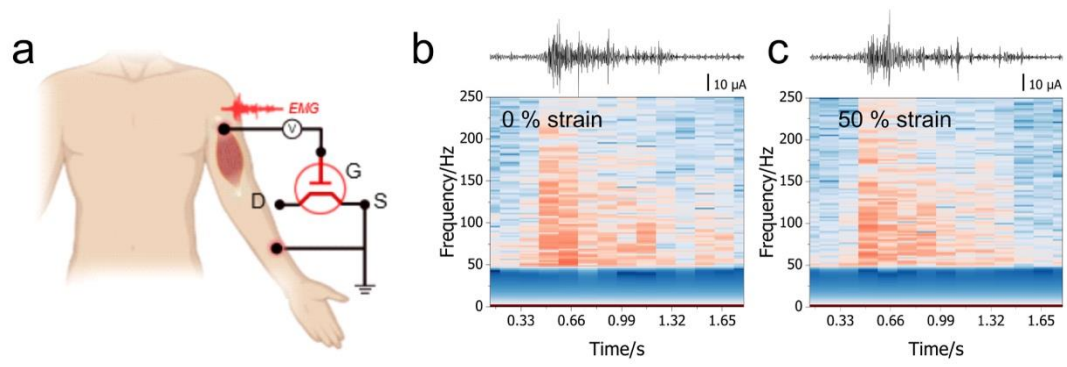
Supplementary figure 24. EMG recording with ISOECTs. (a) Schematic showing the circuit diagram of using ISOECT for on-body EMG recording. **(b)** The EMG signal (top) and the recorded time-frequency spectra (bottom) under strain of 0% and 50%.
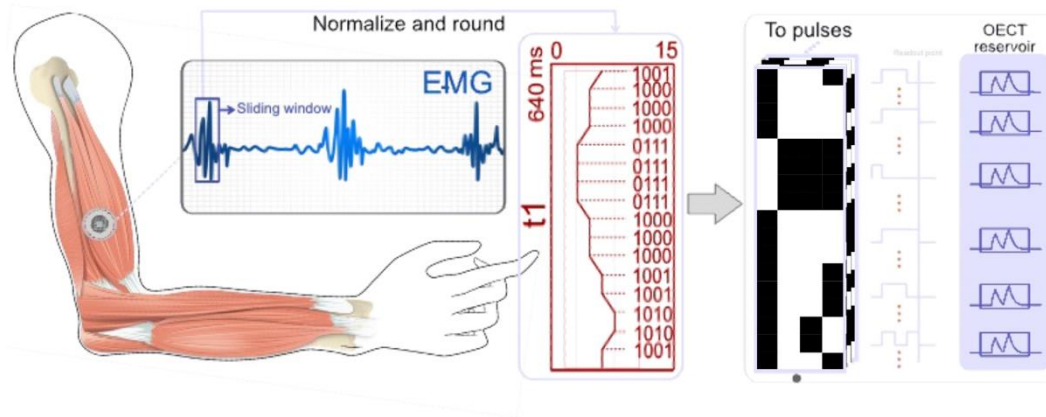
Supplementary figure 25. Preprocessing of the EMG signals. To process the EMG data and make it compatible with the computing system, the following steps are performed. First, the raw EMG data collected from the sensors was standardized by subtracting the mean of all signals and then divided by the standard deviation of all signals. Next, the standardized data was normalized to a range of 0-15, corresponding to binary values 0000-1111, where 0 represents the low level and 1 represents the high level. This transformation optimizes the data for subsequent calculations. To further reduce the data size, a sampling window with a width of 640 ms (640 data points) was defined.
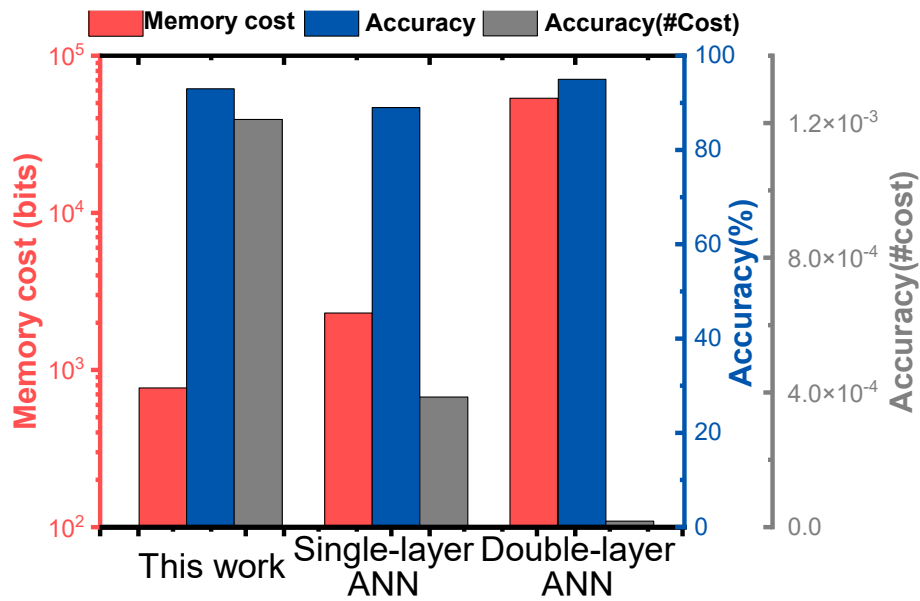
Supplementary figure 26. Comparison of the memory cost, and accuracy between our ISOECT RC system, a single-layered ANN, and a double-layered ANN.

Reference

1   Du, C. *et al.* Reservoir computing using dynamic memristors for temporal information processing. *Nature Communications* **8**, 2204, doi:10.1038/s41467-017-02337-y (2017).

2   Sun, L. *et al.* In-sensor reservoir computing for language learning via two-dimensional memristors. *Science Advances* **7**, eabg1455, doi:doi:10.1126/sciadv.abg1455 (2021).

3   Milano, G. *et al.* In materia reservoir computing with a fully memristive architecture based on self-organizing nanowire networks. *Nature Materials* **21**, 195-202, doi:10.1038/s41563-021-01099-9 (2022).

4   Zhong, Y. *et al.* Dynamic memristor-based reservoir computing for high-efficiency temporal signal processing. *Nature communications* **12**, 408 (2021).

5   Moon, J. *et al.* Temporal data classification and forecasting using a memristor-based reservoir computing system. *Nature Electronics* **2**, 480-487 (2019).